Fibertract segmentation in position orientation space from high angular resolution diffusion MRI

Patric Hagmann,[a,b,*] Lisa Jonasson,[b] Thomas Deffieux,[b] Reto Meuli,[a] Jean-Philippe Thiran,[b] and Van J. Wedeen[c]

[a]Department of Radiology, Lausanne University Hospital (CHUV), Switzerland
[b]Signal Processing Institute, Ecole Polytechnique Fédérale de Lausanne (EPFL), Switzerland
[c]Department of Radiology, MGH Martinos Center for Biomedical Imaging, Harvard Medical School, Charlestown, MA 02129, USA

In diffusion MRI, standard approaches for fibertract identification are based on algorithms that generate lines of coherent diffusion, currently known as tractography. A tract is then identified as a set of such lines selected on some criteria. In the present study, we investigate whether fibertract identification can be formulated as a segmentation task that recognizes a fibertract as a region where diffusion is intense and coherent. Indeed, we show that it is possible to segment efficiently well-known fibertracts with classical image processing methods provided that the problem is formulated in a five-dimensional space of position and orientation. As an example, we choose to adapt to this newly defined high-dimensional non-Euclidean space, called position orientation space, an algorithm based on the hidden Markov random field framework. Structures such as the cerebellar peduncles, corticospinal tract, association bundles can be identified and represented in three dimensions by a back projection technique similar to maximum intensity projection. Potential advantages and drawbacks as compared to classical tractography are discussed; for example, it appears that our formulation handles naturally crossing tracts and is not biased by human intervention.
© 2006 Elsevier Inc. All rights reserved.

Introduction

Classically, the question of revealing nerve fiber architecture in the brain, based on diffusion-weighted MR images, is addressed by building lines of coherent diffusion, that are interpreted as axonal trajectories. Such magnetic resonance tractography is usually achieved by solving for some path integral in a field of principal diffusion vectors derived from Diffusion Tensor (DT) MRI data (Basser et al., 2000; Conturo et al., 1999; Mori and van Zijl, 2002; Mori et al., 1999; Wedeen et al., 1996). This approach is now understood to have some significant limitations (Basser et al., 2000; Lazar and Alexander, 2003; Tournier et al., 2002), chief among them is its inability to image fiber crossings (Mori and van Zijl, 2002; Wiegell et al., 2000). Several methods, probabilistic and deterministic, were devised to improve the effects of this limitation of DTI on tractography (e.g., Behrens et al., 2003; Hagmann et al., 2003; Lazar et al., 2003; Poupon et al., 2001), but none has proven to be wholly satisfactory, as none is able to robustly provide accurate and objective images of tract intersections. It is now generally accepted that the orientational information provided by the DT model is insufficient to accurately map important and critical brain areas (Hagmann et al., 2004; Wedeen et al., 2005). Moving beyond the tensor model, new representations, now existing, consider the pattern of diffusion in each voxel in terms of its orientational distribution of diffusion intensity (orientation density function, ODF). These methods include diffusion spectrum MRI (DSI) (Wedeen et al., 2000, 2005), Q-ball (Tuch et al., 2003) and related "high angular resolution diffusion imaging" MRI methods which map the angular variation of the probability density function (PDF) using more limited encoding schemes (Jansons and Alexander, 2003a,b; Tournier et al., 2004; Zhan et al., 2004). On such data, it has been shown that MRI tractography is now able to accurately map important fibertracts as the cortico-spinal tract or the corpus callosum, while keeping the important directional information at fibre crossing sites (Hagmann et al., 2004).

If the anatomy of a tract or bundle of fibers needs to be described, a common solution consists in placing regions of interest (ROIs) over some particular brain areas and to extract the lines that pass through such ROIs. A more subtle way is to consider a fibertract as a set of those lines that share some geometrical property, like having similar shape and position (Brun et al., 2004) or being adjacent over long distances (Jonasson et al., 2005c). However, a fiber tract is not only a set of axons. It can also be seen as a single object with a rather precise boundary with a given shape and volume (Jones et al., 1999). For example, the arcuate fasciculus is a semi-toric or crescent shaped object with a volume

---

* Corresponding author. Lausanne University Hospital (CHUV), CH-1011 Lausanne, Switzerland.
E-mail address: Patric.hagmann@epfl.ch (P. Hagmann).
Available online on ScienceDirect (www.sciencedirect.com).

that depends on gender, handedness and the hemisphere considered (Hagmann et al., 2006). In terms of diffusion, as will be discussed further down, such an object is a region of coherent diffusion as the nerve fibers run mainly parallel within the tract (Beaulieu, 2002).

We have mentioned that the advent of diffusion MRI data of higher angular resolution (DSI, Q-ball, etc.) enables tractography to handle naturally fiber trajectories in regions of fiber-crossing, essential prerequisite to accurately map connectivity. Furthermore, as we will show hereafter, high angular resolution allows representing diffusion as a signal (or a scalar field) mapped on a five-dimensional space of position and orientation. This is important as standard image processing tools can be readily applied provided that they are adapted for this high-dimensional non-Euclidean space. Accordingly, we will see how tract identification can be reformulated as a segmentation problem on a five-dimensional space and solved with classical image segmentation algorithms. In such a space, fibertracts are represented as disjoint clusters where crossing fiber tracts are disentangled. For illustration, we show results obtained by adapting a classical segmentation method based on the hidden random Markov field formalism.

Material and method

Theory

What is the position orientation space (POS)?

In diffusion imaging of high angular resolution, such as Diffusion Spectrum Imaging or Q-ball imaging, data are represented by an ODF in every position. The ODF is a two-dimensional function on the unit sphere whose values describe the diffusion intensity in each orientation $u(\theta, \varphi)$. This ODF is actually a radial projection of the full three dimensional diffusion function or diffusion spectrum ($\bar{p}_\Delta$) (Wedeen et al., 2005):

$$\text{ODF}(u) = \int_{\mathbb{R}^+} \bar{p}_\Delta(\rho u)\rho^2 d\rho, \tag{1}$$

with $\|u\| = 1$ and ρ the integration radius. For the purpose of the present segmentation application, the ODF is normalized such that its maximum value is 1. We refer to the sphere on which the ODF is defined as the orientation space whereas $\mathbb{R}^3$ is the position space. A diffusion MRI dataset provides for any given position voxel $r(x, y, z)$ and for every orientation $u(\theta, \varphi)$, a diffusion intensity.

Instead of considering those two spaces separately, we merge them into a unique space. Intuitively, this new space is a tensor product between the three-dimensional Euclidean position space $\mathbb{R}^3$ and a two-dimensional orientation space—the 2D sphere—resulting in a five-dimensional space whose coordinate system is ($s = [r, u], r \in \mathbb{R}^3, u \in$ 2D sphere) (Figs. 1A and B). Diffusion is then simply a scalar field mapped on this space. This intuitive description of POS must now be formulated precisely.

Defining position orientation space

Let us first consider a set **S** as:

$$\mathbf{S} = \{s = (r,u); r \in \mathbb{Z}^3,$$

$$u \in \{N \text{ elements distributed over the 2D sphere}\}\}. \tag{2}$$

We introduce directly a discrete set because it fits naturally the sampled MRI data (through the discrete measurements) and suits the segmentation formalism that we will choose. However, an equivalent continuous set can be constructed if necessary by defining $r \in \mathbb{R}^3$, $u \in$ 2D continuous sphere. Each element of the space is called a site s and is identified by its coordinates of position and orientation (r_s, u_s).

Lets define the function δ of two sites s and s' :

$$\delta(s,s') = \|r - r'\| + \gamma \widehat{u,u'} \tag{3}$$

where $\widehat{u,u'}$ is the solid angle between vectors u and u' . γ is a constant weighting the angular distance as compared to the Euclidean distance. We choose $\gamma = 18/\pi$ to make a unit of angular distance equal to 10°.

We notice that the function $\delta(.,.)$ on the set **S** is a metric since it satisfies the three basic properties of symmetry and identity condition as well as the triangle inequality (see Appendix). Hence, the metric δ induces a topology on the set **S** whose closed sets over all subsets can be realized as the intersection of closed balls defined as:

$$\mathbf{B}_\rho(s) = \{s' : \delta(s,s') \le \rho\} \tag{4}$$

with $s \in \mathbf{S}$ and $\rho \in \mathbb{R}^+$. A closed ball of radius ρ and centered on the site $s(\mathbf{B}_\rho(s))$ is a set of points that are at a distance smaller or equal to ρ from s.

Defining POS formally has two obvious positive consequences. The first is that POS is a metric space (δ,**S**) which is a useful property for signal processing (Sochen et al., 1998). Second, it allows defining a neighborhood on POS very easily, which will be used in our segmentation model.

The neighborhood of a site $s \in \mathbf{S}$ is chosen as follows:

$$\mathbf{N}_s = \mathbf{B}_3(s) \backslash \{s\} \tag{5}$$

This simply means that the neighbors of a site s are all the sites that are within a distance less or equal to 3 from s in POS.

The set $\mathbf{N} = \{\mathbf{N}_s\}_{s \in \mathbf{S}}$ defines a neighborhood system for **S** (Fig. 1C) since it satisfies the two properties (Geman, 1990; Geman and Geman, 1984):

- $s \notin \mathbf{N}_s, \forall s \in \mathbf{S}$
- $s \in \mathbf{N}_{s'} \Leftrightarrow s' \in \mathbf{N}_s, \forall (s,s') \in \mathbf{S}^2$

Eq. (3) defines a distance that is simple and natural. The distance between two points is a weighted sum between the distance in position (the natural physical distance) and the angular distance between both orientations.

Getting to know the POS

In order to get some intuition on POS, let us consider the problem in two dimensions instead of three, hence defining a 3D POS (x, y, θ) instead of the actual 5D POS $(x, y, z, \theta, \varphi)$. As depicted in Fig. 2A, we consider two fibertracts (yellow and red) that cross at $\approx 30°$ in the $x-y$ plane. The underlying diffusion pattern is represented by the ODF map in the same plane. We see that in the crossing areas the ODFs exhibit two directional maxima tangent to both fiber tracts. In Fig. 2B, where we have isolated both individual tracts, we readily see that they overlap in the middle of the image, reason why it is impossible to separate crossing tracts in the 2D position space. We now add a third dimension, which we call $\theta = \arccos(u \cdot [1, 0])$, that codes for the angular variable of the ODF with reference to the x axis, its orientation. Intuitively, we define this space as the 3D POS. The ODFs of Fig. 2A are then mapped as a scalar field $d(x, y, \theta)$ of
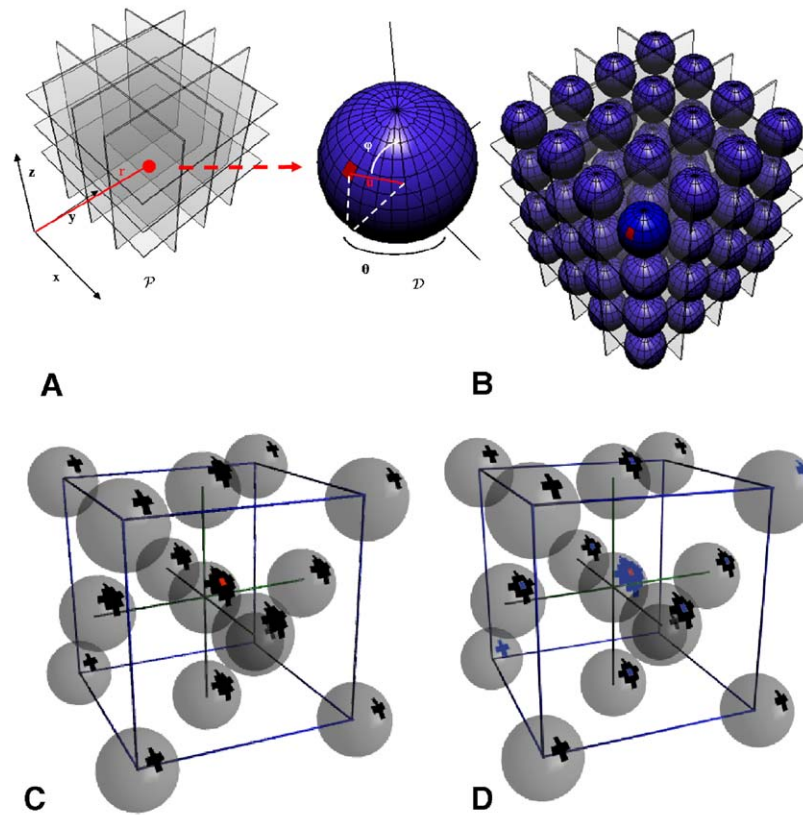
Fig. 1. Position orientation space. (A) Schematic representations of the three-dimensional Euclidean position space (left) and the two-dimensional orientation space (right) existing for every position r. (B) The space resulting in the merging of both the position space and the orientation space is represented with a sphere in every position. One of the sites $s = (r_s, u_s)$ of the space has been painted in red. (C) illustrates the neighborhood. The neighbors of the current site s in red are black ($\mathbf{N}_s = \mathbf{B}_3(s) \backslash \{s\}$). The number of angular neighbors on each voxel decreases with its spatial distance from the center. (D) The subset $\mathbf{K}_s$ of the neighborhood $\mathbf{N}_s$ is used to inject a priori on the shape of the object. Only neighbors "aligned" with the current site are selected in $\mathbf{K}_s$. This favors diffusion homogeneity along the fibertract.

diffusion intensity on 3D POS. The green interfaces of Fig. 2C represent iso-surfaces of the scalar field ($d(x, y, \theta) =$ constant)). Whereas both tracts where overlying structures in two dimensions, we see that in 3D POS they nicely disentangle. At this stage, we would just like to emphasis that for representation purposes the 3D POS looks Euclidean on our 3D plot, but by no means it is, as there is periodicity along θ.

A proposal of segmentation of POS in two classes

In POS fiber tracts correspond to beams of intense diffusion (Fig. 2)—i.e., they lie in regions where the diffusion scalar field $d(r, u)$ takes high values along a preferential direction—whereas one may not associate tracts to areas of low diffusivity. The aim of the segmentation task is to label every POS site as "1" if it corresponds to a position inside a tract or with "0" if it lies outside, i.e., we want to compute and indicator field on POS.

We are now able to make the link with classical image segmentation formulations. Many segmentation algorithms can potentially be adapted. However, given the size of the dataset we need to choose an efficient approach. For illustration purpose, we choose to adapt a well-known, rather robust method that has the additional advantage that it is able to segment all the objects of the scene at once free of human interaction. The Markovian approach in image denoising and segmentation, first introduced by (Geman,

1990; Geman and Geman, 1984), is powerful and now a widely accepted paradigm. It has the advantage of providing lots of flexibility while keeping implementation simple. Markov Random Fields are convenient to describe the dependence of one site upon its neighborhood. This is usually done to add a priori in an image model and uses the probabilities to model such dependence. The idea is to consider the data as an observed field, which results from the noisy measure by an imaging device of some true, yet not directly observable reality (i.e., the fibertracts), called the hidden field. It can be guessed from its dependence upon the observed field and its neighborhood values.

Our goal here is to perform a segmentation; this needs to be kept in mind when defining the image model and the probabilities. We will have to favor homogenous, contiguous and high diffusivity regions and label them as a tract. We will see the hidden random field as the ideally segmented image and generate the most probable configuration with respect to the measured diffusion values.

Practically, we derive our formulation from the Markov Random Field Maximum A Posteriori (MRF-MAP) classification algorithm proposed by Zhang et al. (2001) that was designed to segment T1-weighted MRI images. Accordingly, we reformulate the neighborhood system in accordance to the particular topology of POS and the energy functions in order to fit our image model.
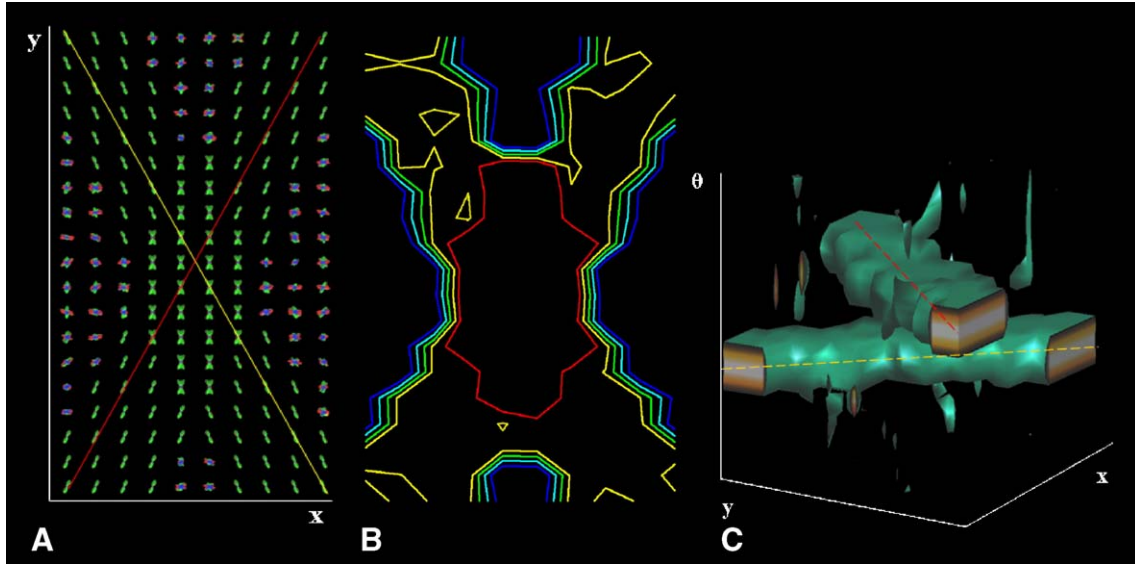
Fig. 2. Model of crossing fibertracts in two dimensions. (A) ODF map of 2 crossing fibertracts at ≈30° in the plane with a noisy background. (B) In two dimensions, the region of fiber-crossing is shared by both tracts, the two objects, are entangled. (C) An associated 3D POS is constructed by adding to the two dimensions of position a third dimension that codes for the angular orientation of diffusion. Accordingly, the ODF map is mapped into a scalar field $d(x, y, \theta)$. A fiber tract which is a region of intense coherent diffusion corresponds, in this space to an intense beam, represented here by a green iso-intensity surface. We readily see that as both tracts do not have their maximal diffusion in the same orientation they disentangle nicely in POS. The isolated small vertical patches are a translation of the noise in the data and illustrate the necessity for the regularization procedure (in our case, the Gibbsian formalism).

Let us consider the discrete diffusion scalar field reconstructed from the MRI data:

$$\mathbf{S} \rightarrow \mathbf{D}$$
$$(r,u) \mapsto d(r,u)$$

as a realization y of some random field Y which models the random variable generating the MRI data ($y_s \equiv d(r_s, u_s)$). Y is the observed random field, and it takes its values in the configuration space:

$$\mathbf{Y} = \left\{ y = (y_1, \ldots, y_{|\mathbf{S}|}) : y_s \in \mathbf{D}, \ s \in \mathbf{S} \right\} \tag{6}$$

where $\mathbf{D} = \{0, 1, \ldots, D\}$ is the set of values that the diffusion scalar field can take. In simple terms we can think of each configuration y of the configuration space $\mathbf{Y}$ as one possible diffusion MRI data set over all possible data sets. Given that y is the observed field, we know that its true configuration is in fact the acquired MRI data.

We furthermore consider a random field X taking its values in the configuration space:

$$\mathbf{X} = \left\{ x = (x_1, \ldots, x_{|\mathbf{S}|}) : x_s \in \mathbf{L}, \ s \in \mathbf{S} \right\} \tag{7}$$

with $\mathbf{L} = \{0, 1\}$ and $|\mathbf{S}|$ being the number of elements in the set $\mathbf{S}$ (number of sites). Each configuration x represents an indicator field of fibertracts, where sites that lie in within a fibertract take value "1" and sites free of tract value "0". We can think of a specific configuration x as a kind of ideal ODF map, where in each position, the ODF would have the shape of one or several compass needles pointing in the direction of the fibertract. We call X the hidden random field as it is not directly observable but considered to be the physical cause of the measured observed field Y and therefore can be guessed from a realization of Y.

Obviously X is not independent of Y and X_s is not independent of its neighborhood; let us formalize these concepts. We consider that there is a local spatial correlation in X, property that can be modeled by a Markov Random Field. Accordingly, a neighborhood system must be defined, and we naturally use the system that we defined above to generate the POS: $\mathbf{N}$. It follows that the local characteristic of X can be expressed as: $p(x_s | x_{\mathbf{S} \setminus s}) = p(x_s | x_{\mathbf{N}_s})$, meaning that the dependences are only local. The diffusion value at one site x_s is only dependent on its neighbors $\mathbf{N}_s$ and not on all the POS. Furthermore, we specify the relation between X and Y by assuming that these random fields are related in the following way:

$$p(y|x) = \prod_{s \in \mathbf{S}} p(y_s | x_s) \tag{8}$$

which states that conditionally to a given configuration $x \in \mathbf{X}$ the random variables Y_s are independent.

The image classification problem we consider involves assigning to each POS site a class label belonging to the set $\mathbf{L}$. We look for the true but unknown configuration x that has generated the observation y; it can be estimated by maximizing the probability $p(x|y)$.

According to the Maximum A Posteriori (MAP) criterion, this objective can be formalized with the following optimization task, where $p(y)$ is obviously constant:

$$\hat{x} = \arg \max_{x \in \mathbf{X}} \{ p(y|x) p(x) \} \tag{9}$$

and where x is the best estimate given the observation y.

According to the Gibbs-Markov equivalence (p. 260, Brémaud, 1999) and more particularly to the Hammersley–Clifford theorem (Hammersley and Clifford, 1968), the distribution of a Markov Random Field can be expressed as a Gibbs distribution. Hence,

$$p(x) = \frac{1}{Z} e^{-U(x)} \tag{10}$$

where the energy function U derives from a Gibbs potential (p. 258, Brémaud, 1999) and Z is a normalizing constant called the partition function.

Furthermore, because of the conditional independence stated above (8), it is always possible to write $p(y|x)$ as a Gibbs distribution:

$$p(y|x) = \frac{1}{Z'} e^{-U(y|x)} \tag{11}$$

Consequently (10) is equivalent to minimizing the negative log-likelihood:

$$\hat{x} = \arg \min_{x \in \mathbf{X}} \{U(y|x) + U(x)\}. \tag{12}$$

Gibbsian distributions give us considerable flexibility for shaping the probabilistic relationships between the individual components of the random field. As such, we choose convenient and easy to implement potentials in the definition of the energy functions. We model the conditional energy as

$$\begin{aligned} U(y|x) &= \alpha \sum_{s \in \mathbf{S}} U_s(y_s|x_s) \\ &= \alpha \sum_{s \in \mathbf{S}} \left\{ (y_s - t) 1_{[x_s = 0]} + (t - y_s) 1_{[x_s = 1]} \right\}. \end{aligned} \tag{13}$$

where t is a threshold value experimentally chosen between 0 and 1. $1_{[\cdot]}$ is the indicator function, taking value 1 if the statement in brackets is satisfied and 0 otherwise; α is a tuning parameter chosen to be 1. These potentials $U_s(y_s|x_s)$ are made to favor the state "fibertract = 1" in regions of high diffusivity and reversely favor the state "no-fibertract = 0" in regions of low diffusivity. With a typical value of t around 0.5 and with y_s ranging from 0 to 1, we can see that a high value of y_s will lead to a smaller energy and thus a more stable configuration if x_s is equal to 1 (if $y_s > t$ then $t - y_s < y_s - t$), conversely a low value of y_s will lead to a more stable configuration if x_s is chosen to be 0.

While the conditional energy ($U(y|x)$) is made to link the segmentation result to the measured data, the prior energy ($U(x)$) is designed to shape the result according to our a priori model. As such, we chose potentials that favor homogeneous and oriented regions by minimizing the quadratic distance with all the neighboring values which is the same as computing the mean diffusion value over the neighborhood (the mean is the value minimizing the quadratic error within a given set). However, instead of computing this mean value over the whole neighborhood $\mathbf{N}_s$, which is isotropic, we choose to only use the values in an anisotropic subset $\mathbf{K}_s$ of the neighborhood $\mathbf{N}_s$ (Fig. 1D). Sites that are aligned in terms of position to the current site orientation have a higher probability of being part of the same fibertract and thus are taken into account to favor homogeneity. Sites that do not belong to the subset $\mathbf{K}_s$ are likely not to belong to the same fibertract and thus are not taken into account.

There are several ways to define $\mathbf{K}_s$. We define it in a similar way than $\mathbf{N}_s$ in Eqs. (3), (5) using this time a semi-distance function $f(\cdot)$ which is minimum for sites whose orientations u and u' match their spatial alignment $r - r'$:

$$\begin{aligned} f(s,s') &= \| r - r' \| \\ &+ \eta \widehat{u,u'} + \mu(\widehat{u,(r-r')} + \widehat{u',(r-r')}) \end{aligned} \tag{14}$$

with $\eta = 18/\pi$ and $\mu = 9/\pi$ and where the last term is the solid angle between the orientations of the sites and their spatial alignment and is minimum when u, u' and $(r-r')$ share the same direction.

We then define the subset $\mathbf{K}_s$ (Fig. 1D) in analogy to (5) as:

$$\mathbf{K}_s = \{ s' \in \mathbf{N}_s : f(s, s') \leq 3 \} \tag{15}$$

Figs. 1C and D illustrate quite nicely the difference between $\mathbf{N}_s$ and $\mathbf{K}_s$. The prior energy is then defined as the mean on the subset $\mathbf{K}_s$:

$$U(x) = \beta \sum_{s \in \mathbf{S}} U_s(x_s|x_{N_s}) = \sum_{s \in \mathbf{S}} \frac{1}{|\mathbf{K}_s|} \left\{ \sum_{r \in \mathbf{K}_s} 1_{[x_r \neq x_s]} \right\} \tag{16}$$

where β is a tuning parameter that must be chosen empirically and $|\mathbf{K}_s|$ the number of elements in the subset $\mathbf{K}_s$, defined in Eq. (15). This ensures that the configuration $x_s = 0$ will be more stable if there is already a lot of 0 in $\mathbf{K}_s$ and that the configuration $x_s = 1$ will be more stable if there is a lot of 1 in $\mathbf{K}_s$, thus favoring homogenous region.

Although mathematically simple, this type of MAP problem can be computationally difficult because of combinatorial explosion. We use the Iterative Conditional Modes (ICM), algorithm proposed by Besag (1986), that uses a "greedy" strategy by performing local minimization iteratively and is known to converge after only a few iterations.

Besag's ICM segmentation algorithm.

For a few iterations

For all sites s of the hidden random field X
    Find the value ($x_s = 0$ or 1) which minimizes $\alpha U_s(y_s|x_s) + \beta U_s(x_s)$
Update x_s
End

Fibertract labeling

We define two separate fibertracts as two clusters in the optimized configuration x that are disjoint with respect to the neighborhood system. To finalize the segmentation, we therefore use an iterative algorithm that scans x and labels the separate clusters uniquely. The labeled clusters are defined on the five-dimensional POS, space which cannot be easily visualized or interpreted. Therefore, each labeled cluster which represents a region of maximal diffusion coherence is back projected into the usual three-dimensional space and represented for example with colored surfaces.

At this stage, we need to make an important conceptual remark. Since diffusion is symmetric with respect to its orientation ($d(r, u) = d(r, -u)$) as shown by Wedeen et al. (2005), it follows that theoretically every object is segmented twice, once in each direction. The POS as presented here has two advantages, first, it is more general, and second, its mathematical properties are simpler. In practice, however, we perform the segmentation only on one hemispace in order to improve computational efficiency.

Acquisition and segmentation parameters

Two data sets were acquired at 3 T with either an Allegra head-scanner (Siemens, Erlangen, Germany) or an Achieva (Philips, Einthoven, The Netherlands) using diffusion weighted single-shot echo-planar MRI multislice technique. The imaging parameters specific to each of the two data sets are summarized in Table 1. The diffusion-weighted images were acquired according to the classical DSI scheme as described in (Wedeen et al., 2005). Briefly, at each location, diffusion-weighted images were acquired for $N = 515$ values of q-encoding, comprising in q-space the points of a cubic lattice within the sphere of 5 lattice units in radius.

$$q = aq_x + bq_y + cq_z, \tag{17}$$

Table 1
Summary of acquisition parameters

MRI type	Siemens Allegra 3T	Philips Achieva 3T
Data set	Right hemibrain	Brainstem
Diffusion pulse sequence	Twice refocused spin echo (Reese et al., 2003)	Standard pulsed gradient spin echo
Matrix size × number of slices	$64 \times 64 \times 32$	$128 \times 128 \times 24$
Voxel dimension [mm]	$3.8 \times 3.8 \times 3.8$	$2.8 \times 2.8 \times 2.8$
TE/TR [ms]	156/3000	154/3000
Δ/δ [ms]	66/60	47.6/35
g_{max} [mT/m]	40	80
b_{max} [s/mm^2]	17,000	12,000
Acquisition time [min]	~25	~60

with a, b, c integers and $\sqrt{a^2 + b^2 + c^2} \leq 5$. q_x, q_y and q_z denote the unit phase modulations in the respective coordinate directions. The diffusion spectrum was then reconstructed by taking the discrete 3D Fourier transform of the signal modulus. The signal is pre-multiplied by a Hanning window before Fourier transformation in order to ensure a smooth attenuation of the signal at high $\|q\|$ values. An ODF map is built by radial projection of the diffusion spectrum (1) and multiplied by the generalized fractional anisotropy (GFA) (Tuch, 2004). Segmentation is performed in a white matter mask that is obtained by thresholding the GFA map. The value of the different algorithm parameters are set experimentally depending on the dataset (see Table 2).

Results

The first study is centered on the brain stem. We choose this part of the brain as there are several well-delimited fibertracts that define the known anatomy of this region. Fig. 3 displays the segmentation results based on the brainstem acquisition in the middle and right column. In the left column, we depict as reference the anatomical structures as reconstructed by DSI-based tractography (Hagmann et al., 2004). On Fig. 3A, we can see the segmented left and right corticospinal tracts in red, structures that are involved in voluntary movement of the body. They travel on this MRI acquisition from the cerebral peduncles down to the cranial part of the spinal chord by passing through the pons. In yellow, we can identify the posterior columns (cuneate and gracile fascicles) that carry on sensitive information from the extremities up the central nervous system. We see the trajectory that these fibers take on the tractography result on the left image. We can see that the segmentation algorithm captures the core portion of the tract. Fig. 3B displays the cerebellar peduncles. They connect the cerebellum with the vestibular nuclei located in the lower pons and the spinal chord: these peduncles are represented in blue. DSI tractography (left image) as well as POS segmentation captures these structures although it seems that the cerebellar extremities that fan out are only captured by tractography. The middle cerebellar peduncle is the largest of the peduncles and links the cerebellum with the pons. Segmentation captures well the body of this tract on each side that is displayed in green. We see that the most medial part of the peduncle that lies in the middle of the pons is not captured, the reasons of this phenomenon will be discussed further down. The superior cerebellar peduncle connects the cerebellum to the midbrain and contains efferent fibers from different cerebellar nuclei. It is depicted in white in Fig. 3C.

This tract nearly lies onto the posterior columns in its cranial portion, thus building a kissing tract situation as commonly referred to in the tractography jargon when two tracts come together and run parallel for a while. This situation has an influence on the segmentation result.

The second data set that has been studied is centered on one brain hemisphere. The largest structure segmented is the corona radiata. Under this term, one means a set of fiber bundles that take their origin or end in the brain cortex and pass through the pons. Among these tracts, there is the corticospinal tract, the fronto-pontine tract and the parieto-temporo-pontine fibers. With our segmentation algorithm the corona radiata is identified as one blue structure in Fig. 4A. Indeed in the brainstem, these different bundles share the same position and the same orientation in the brainstem alike the root of a sheaf of twigs. Cortico-cortical connections are widespread, and they form for most of them loose association bundles that are variable in size and shape. However, some association bundles have got a tight and well-defined body. In Fig. 4B, we can identify the cingulum bundle in yellow, it is a structure the belongs to the limbic system and travels anterior–posteriorily in a parasagittal plane just above the corpus callosum in the cingulated gyrus. The arcuate fasciculus that travels between the frontal to the temporal lobe via parietal structures and the inferior longitudinal fasciculus that connects the temporal with the occipital lobe share some sites in position orientation space. This explains the reconstruction from our algorithm that identifies these structures as one light green object. On the same image, the uncinate fasciculus is represented in dark green. This structure that connects the temporal with the frontal lobe clearly separates from the inferior temporal fasciculus as its orientation is nearly perpendicular in the tip of the temporal lobe. On Fig. 4C, we see the relationship between the root of the corona radiata (dark blue) and the posterior column (light blue) as well as the superior (light yellow) and mid cerebellar (dark yellow) peduncles at the level of the pons. Finally, in red, the algorithm has segmented the compact component of the corpus callosum (Fig. 4D). Fig. 4E is a coronal cut trough the centrum semi ovale. An ODF map represents diffusion in a usual fashion, and a section through the different objects is depicted. We see how different structures share partly the same 3D volume as their surrounding surfaces overlap. For example, it is clear that the arcuate fasciculus crosses the corticospinal tract (i.e., blue and green surface). The same observation is valid for the cingulum and the callosal fibers (red and green surface) as well as corticospinal and callosal fibers.

Discussion

The enormous success of DTI has somehow sealed up the idea that diffusion is a tensor field or in other words a mapping

Table 2
Chosen tuning parameters of the algorithm

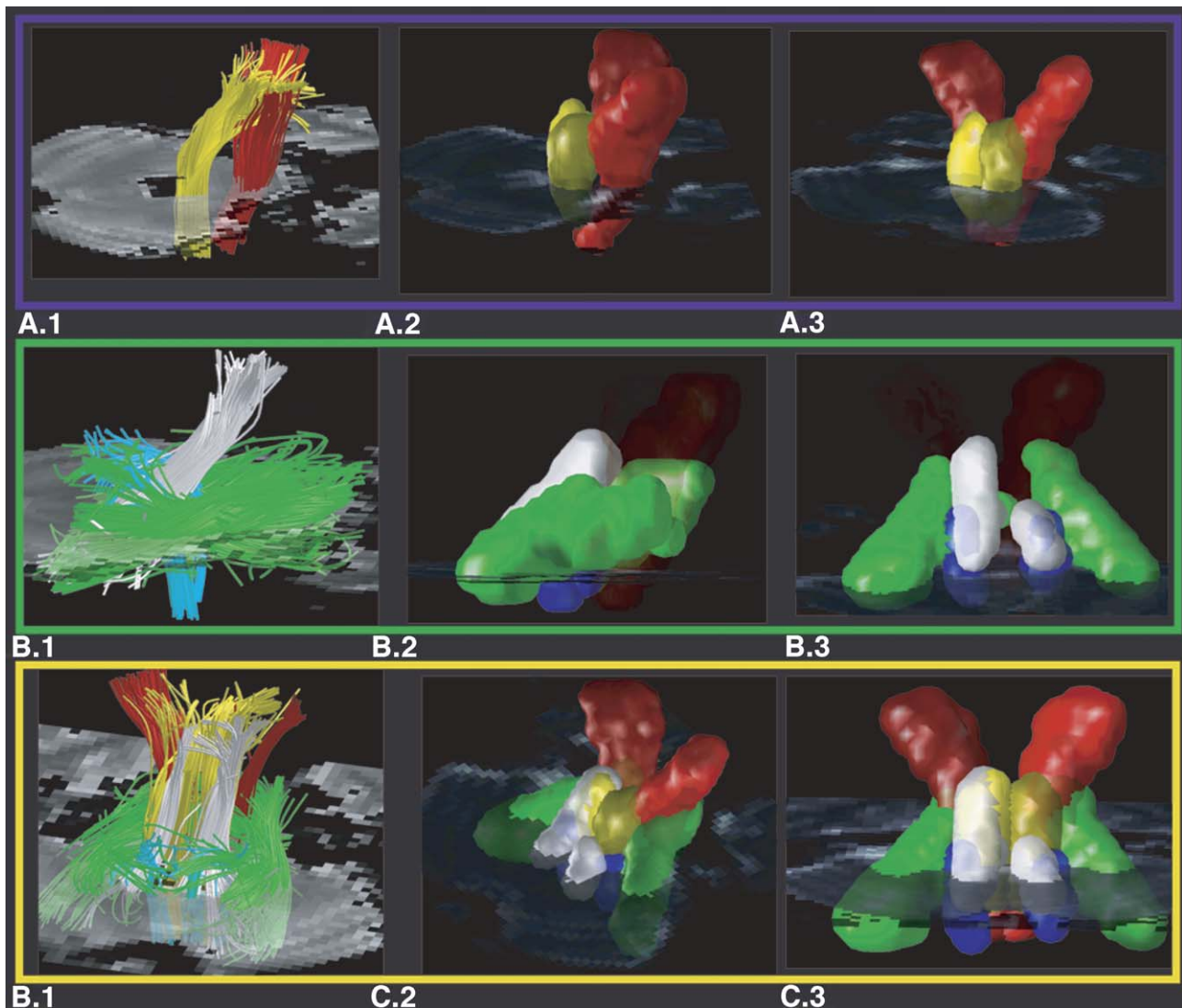| Data	Hemibrain	Brainstem
t	0.4	0.65
α	1	1
β	1.25	1.5
Number of iteration(s)	2	1

Fig. 3. Brainstem fibertracts. First column DSI streamline tractography (Hagmann et al., 2004). Second and third column are the comparative segmentation results. (A) Corticospinal tract in red, posterior columns (cuneate and gracile fascicles) in yellow. (B) Inferior (blue), middle (green) and superior (white) cerebellar peduncles. (C) Overall relationships between all these structures.

from the three-dimension position space to a set of 6 or 9 values (the DT). Accordingly, it has obscured the fact that the DT is nothing else than a parametric representation of a low pass filtered function defined on the sphere (the orientation space) or even more a low pass filtered three-dimensional diffusion function (Wedeen et al., 2005). Recently, the advent of diffusion techniques with better angular resolution motivated new parametric representations (Tuch et al., 2002) that seem in many respect unsatisfactory as fairly heavy in terms of computation and limited in the spectrum of possible representations. At this point, it seems rather tempting to represent diffusion in a non parametric way. We have seen in this paper that it can be achieved very simply by defining diffusion as a scalar field defined on a five-dimensional position orientation space. Our approach has also some implications on the definition of tractography and fibertract segmentation. Indeed, it is commonly considered as a modelling procedure that aims at filling the gap that exists between diffusion measurements and axonal trajectories. In our opinion, however, it can naturally

be thought of as a simple projection imaging technique based on diffusion data. Indeed, in POS a fibertract corresponds to a beam of intense diffusion (see Fig. 2) that is back projected into the usual three-dimensional position space and represented by a colored iso-surface. Here, we emphasize the goal of any projection technique which is to ease the visualization of higher dimensional data (example maximum intensity projection in angiography). In this framework, fibertract segmentation is just a denoising technique.

Defining diffusion as a scalar field has also another very attractive consequence which is to make it accessible to all the traditional image processing tools that are usually designed for scalar fields defined on a two or three-dimensional Euclidean space. Here, as an example, we have adapted the hidden Markov random field formalism to regularize and segment the data. In this sense, our approach is not very different to the idea of (Zhukov et al., 2003) that applied segmentation to DTI in order to separate the white matter from the remaining gray matter and cerebro-spinal fluid using fractional anisotropy
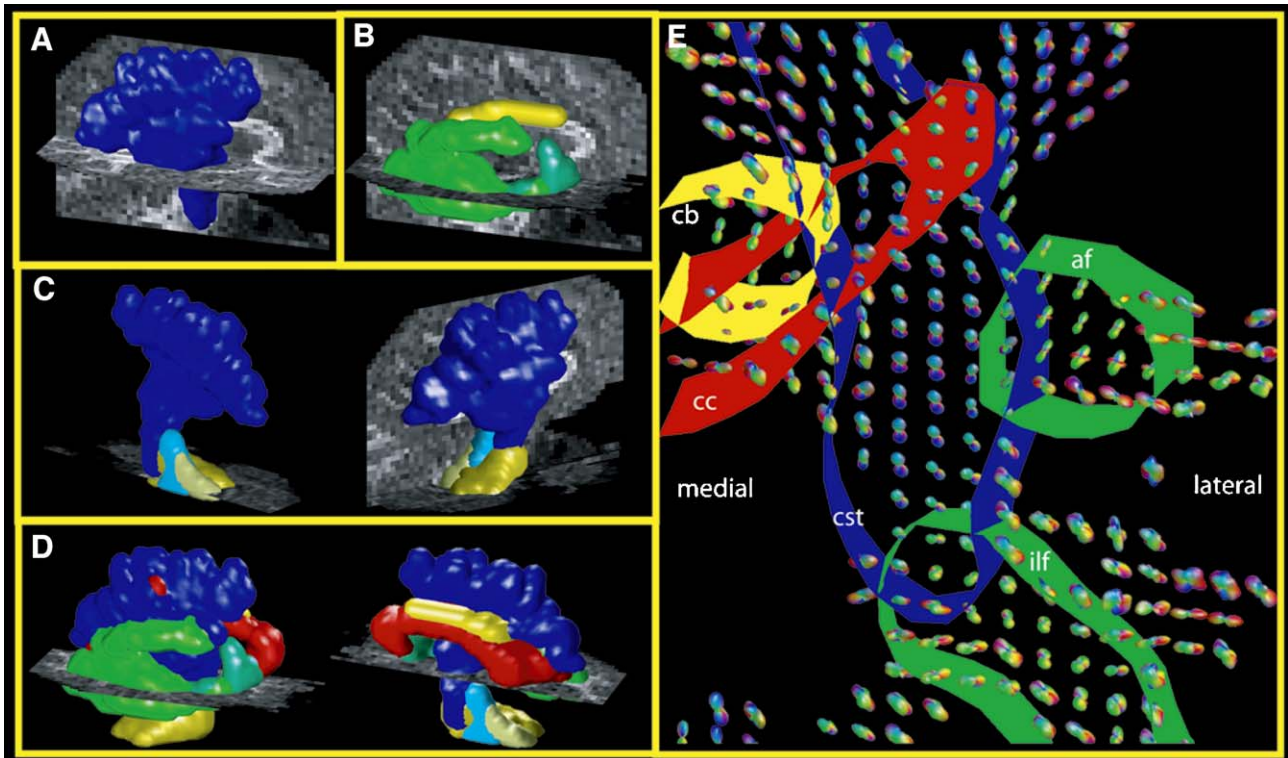
Fig. 4. Segmentation results of fibertracts in the right hemisphere. (A) The corona radiata is isolated in blue. It is made of the corticospinal tract, the fronto-pontine tract and the parieto-temporo-pontine fibers. (B) Is isolated: the cingulum bundle in yellow, the arcuate fasciculus with the inferior longitudinal fasciculus together in green. The uncinate fasciculus in dark green. (C) The intricate relationship is demonstrated between the root of the corona radiata (dark blue) and the posterior column (light blue) as well as the superior (light yellow) and mid cerebellar (dark yellow) peduncles at the level of the pons. (D) All the above structures are depicted together with the corpus callosum in red. (E) depicts a coronal section trough the centrum semi ovale with ODF map representing diffusion and sections through the different objects. Different structures share partly the same 3D volume as their surrounding surfaces cross. For example the corticospinal tract (cst) mixes with the arcuate fasciculus (af) and the inferior longitudinal fasciculus (ilf). The corticospinal tract (cst) also overlaps with the cingulum bundle (cb) and the corpus callosum (cc). The corpus callosum (cc) crosses the corticospinal tract (cst) in the centrum semi ovale.

images. However, as orientational information of the DT is not used, no specific tract can be identified with its method. More recently, Jonasson et al. (2005a) have incorporated orientational information of DT-MRI data to sub-segment brain white matter into main cores of non-overlapping fiber tracts by a three-dimensional geometric flow algorithm. Consequently, regions corresponding to core fibertracts could be segmented, which is a first step in white matter region identification. But at the same time, the method is unable to represent white matter regions of crossing tracts. The typical example is the cortico-spinal tract and the corpus callosum—obviously two separate objects—that at the level of the centrum semi-ovale, overlay in three-dimensional space. We see that the limitations of these techniques are twofold. First, DT-MRI does not provide sufficient angular resolution to resolve crossing fiber populations and secondly formulating the segmentation problem in 3D Euclidean space is unnatural as the objects looked for are entangled in such a representation. This is where it becomes obvious that it is not the segmentation algorithm that is essential but much more the space in which the problem is formulated. In this sense, initial work has already be done on POS fibertract segmentation by adapting level set methods (Jonasson et al., 2005b).

While the topology of POS is naturally given, the Markovian methods provide extensive flexibility to introduce appropriate a

priori information in the regularization and segmentation process. In the particular case of tractography anisotropic prior seems to be useful as it facilitates the identification of elongated objects. However, the level of anisotropy (parameter μ) that has to be introduced on the local energy is a difficult parameter to set. Indeed, too much anisotropy will only capture straight objects while little anisotropy will capture tracts that curve in a tight manner but also allow fusion of tracts that cross at shallow angles.

This directly raises the discussion on the limits of the method. The clustering methods on fibers like (Brun et al., 2004; Jonasson et al., 2005c) are able to separate two tracts that may be close in a little region of POS but far apart on most of their trajectories, as such methods use global information. Our segmentation formulation as it is presented here considers such two tracts (example: two tracts that cross at a shallow angle or diverge at some point) as one single object if the angular contrast is weak, which may be problematic in some brain areas. A good example among our results is the pair made of the inferior longitudinal fasciculus and the arcuate fasciculus. These tracts are over most of their trajectories separate but meet in position and orientation in the tip of the temporal lobe, reason why they are considered as a single object.

Another important point is that a region based approach allows not to measure the "connectivity" between A and B or the trajectory of a single "axon", and in this sense, it is not a tractography method in the classical sense but more a fibertract identification method

capturing regions of coherent diffusion. Instead, it is a powerful method that does not need any ROI placement, and it identifies all tracts in a brain in one shot, independently of the number. It further provides a natural representation for anatomical characterization such as shapes and volumes of such objects or tracts. It may also prove useful for performing tract-specific quantitative measurements, like fractional anisotropy and mean diffusion for example in Wallerian degeneration (Pierpaoli et al., 2001), multiple sclerosis (Filippi et al., 2001) or schizophrenia (Kubicki et al., 2005) as well as in brain maturation studies (Huppi et al., 1998), magnetization transfer (example, Kubicki et al., 2005), in meaningful regions of interest. It may also simply provide a new way to parcelate the brain white matter (examples, Huang et al., 2005; Meyer et al., 1999) as it splits in one shot the brain in a number of significant objects or regions.

We tested our segmentation approach on DSI data, as it is the most principled and validated diffusion MRI technique of high angular resolution (Lin et al., 2003; Wedeen et al., 2005). This technique may currently not be the most appropriate for patient studies as it requires long acquisition times, although this may change rapidly. Fortunately, this segmentation approach can be applied to any diffusion MRI technique that provides ODF maps of high angular resolution, for example q-ball (Tuch et al., 2003) or PAS imaging (Jansons and Alexander, 2003a,b).

In conclusion, we have seen that the advent of diffusion MRI data of higher angular resolution (DSI, q-ball, etc.) enables fibertract identification to be approached efficiently by segmentation methods, provided the problem is formulated in the appropriate space. Extending standard image processing tools, like Hidden Markov Fields, on the five-dimensional and non-Euclidean position orientation space enabled use to segment many tracts of interest in the brain. It provides an interesting alternative to streamline tractography when tract-specific volumetric or quantitative measures are needed.

Acknowledgments

Appendix

Let δ be defined as:

$$\delta(s,s') = ||r - r'|| + \gamma \widehat{(u,u')}$$

with $s = (r, u)$ and $s' = (r', u')$ and $\widehat{(u,u')}$ is the solid angle between u and u'.

Why is δ a distance function?

In order for δ to be a distance on a space **S**, it has to satisfy following three conditions:

$$\delta(s_a, s_b) = 0 \Leftrightarrow s_a = s_b$$
$$\delta(s_a, s_b) = \delta(s_b, s_a)$$
$$\delta(s_a, s_b) \leq \delta(s_a, s_c) + \delta(s_c, s_b)$$

Euclidean distance:

In the first term of δ, we recognize $\delta_E(r, r') = ||r - r'|| = \sqrt{(r_x - r_x')^2 + (r_y - r_y')^2 + (r_z - r_z')^2}$ which is the Euclidean distance and therefore satisfies all of the conditions:

$$||r_a - r_b|| = 0 \Leftrightarrow r_a = r_b$$
$$||r_a - r_b|| = ||r_b - r_a||$$
$$||r_a - r_b|| \leq ||r_a - r_c|| + ||r_c - r_b||.$$

The first two conditions can be easily shown and come from the properties of the scalar product.

The triangle inequality follows from the Minkowsky inequality which states that:

$$\forall p \geq 1, \left(\sum_{k=1}^{n} |a_k + b_k|^p \right)^{1/p} \leq \left(\sum_{k=1}^{n} |a_k|^p \right)^{1/p} + \left(\sum_{k=1}^{n} |b_k|^p \right)^{1/p}$$

which is the triangle inequality for $p = 2$ and $n = 3$.

Spherical distance:

The second part of δ is $\delta_s(u, u') = \widehat{(u,u')} = \arccos(u \cdot u')$, which is simply the angle between unit vectors u and u'. It is known as the great circle distance or spherical distance. As a distance, it also satisfies the following conditions:

$$\widehat{(u_a, u_b)} = 0 \Leftrightarrow u_a = u_b$$
$$\widehat{(u_a, u_b)} = \widehat{(u_b, u_a)}$$
$$\widehat{(u_a, u_b)} \leq \widehat{(u_a, u_c)} + \widehat{(u_c, u_b)}$$

The identity condition can be shown that way:

$$u_a = u_b \Leftrightarrow ||u_a - u_b||^2 = 0 \Leftrightarrow u_a \cdot u_a - 2u_a \cdot u_b + u_b u_b$$
$$= 0 \Leftrightarrow u_a \cdot u_b = 1 \Leftrightarrow \widehat{(u_a, u_b)} = 0$$

The symmetry condition simply follows from the symmetry of the dot product $u_a \cdot u_b = u_b \cdot u_a$.

The triangle inequality follows from the cosines rules for sides (or spherical law of cosines) which state that, in a spherical triangle ABC on a unit sphere of center O:

$$\cos(\widehat{AOC}) = \cos(\widehat{AOB})\cos(\widehat{BOC}) + \sin(\widehat{AOC})\sin(\widehat{BOC})\cos(\widehat{ABC})$$

We know that $-1 \leq \cos(\widehat{ABC}) \leq 1$ thus

$$\cos(\widehat{AOC}) \geq \cos(\widehat{AOB})\cos(\widehat{BOC}) - \sin(\widehat{AOB})\sin(\widehat{BOC})$$
$$= \cos(\widehat{AOB} + \widehat{BOC})$$

Since $\arccos(.)$ is a strictly decreasing function we can write: $\widehat{AOC} \leq \widehat{AOB} + \widehat{BOC}$, which is exactly the spherical triangle inequality.

Back to our distance:

We have $s = (r, u)$ and $\delta(s,s') = \delta_e(r,r') + \delta_a(u,u')$

$$\delta(s_a, s_b) = \delta_e(r_a, r_b) + \delta_a(u_a, u_b) = 0 \Leftrightarrow \delta_e(r_a, r_b) = 0 \text{ and } \delta_a(u_a, u_b)$$
$$= 0 \Leftrightarrow r_a = r_b \text{ and } u_a = u_b \Leftrightarrow s_a = s_b$$
$$\delta(s_a, s_b) = \delta_e(r_a, r_b) + \delta_a(u_a, u_b) = \delta_e(r_b, r_a) + \delta_a(u_b, u_a) = \delta(s_b, s_a)$$
$$\delta(s_a, s_b) \leq \delta_e(r_a, r_b) + \delta_a(u_a, u_b) \leq \delta_e(r_a, r_c) + \delta_e(r_c, r_b)$$
$$+ \delta_a(u_a, u_c) + \delta_a(u_c, u_b) \leq \delta(s_a, s_c) + \delta(s_c, s_b)$$

δ satisfies the three previous conditions and is thus a distance function.

Some references on spherical trigonometry:

Eric W. Weisstein et al. 'Spherical Distance'.

From Mathworld-A Wolfram Web Resource.

http://mathworld.wolfram.com/SphericalDistance.html

Eric W. Weisstein. "Spherical Trigonometry."

From MathWorld-A Wolfram Web Resource.

http://mathworld.wolfram.com/SphericalTrigonometry.html

Smart, 1960, pp. 7–8; Gellert et al. 1989, p. 264; Zwillinger 1995, p. 469.

References

Basser, P.J., Pajevic, S., Pierpaoli, C., Duda, J., Aldroubi, A., 2000. In vivo fiber tractography using DT-MRI data. Magn. Reson. Med. 44 (4), 625–632.

Beaulieu, C., 2002. The basis of anisotropic water diffusion in the nervous system—A technical review. NMR Biomed. 15 (7–8), 435–455.

Behrens, T.E., Woolrich, M.W., Jenkinson, M., Johansen-Berg, H., Nunes, R.G., Clare, S., Matthews, P.M., Brady, J.M., Smith, S.M., 2003. Characterization and propagation of uncertainty in diffusion-weighted MR imaging. Magn. Reson. Med. 50 (5), 1077–1088.

Besag, J., 1986. On the statistical-analysis of dirty pictures. J. R. Stat. Soc. Ser. B Methodol. 48 (3), 259–302.

Brémaud, P., 1999. Markov Chains Gibbs Fields, Monte Carlo Simulation, and Queues. Springer, New York. (444 p.)

Brun, A., Knutsson, H., Park, H., Shenton, M., Westin, C., 2004. Clustering fiber traces using normalized cuts. Medical Image Computing and Computer-Assisted Intervention—Miccai 2004, Pt. 1, Proceedings, vol. 3216, pp. 368–375.

Conturo, T.E., Lori, N.F., Cull, T.S., Akbudak, E., Snyder, A.Z., Shimony, J.S., McKinstry, R.C., Burton, H., Raichle, M.E., 1999. Tracking neuronal fiber pathways in the living human brain. Proc. Natl. Acad. Sci. U. S. A. 96 (18), 10422–10427.

Filippi, M., Cercignani, M., Inglese, M., Horsfield, M.A., Comi, G., 2001. Diffusion tensor magnetic resonance imaging in multiple sclerosis. Neurology 56 (3), 304–311.

Geman, D., 1990. Random-fields and inverse problems in imaging. Lect. Notes Math. 1427, 113–193.

Geman, S., Geman, D., 1984. Stochastic relaxation, Gibbs distributions, and the Bayesian restoration of images. IEEE Trans. Pattern Anal. Mach. Intell. 6 (6), 721–741.

Hagmann, P., Thiran, J.P., Jonasson, L., Vandergheynst, P., Clarke, S., Maeder, P., Meuli, R., 2003. DTI mapping of human brain connectivity: statistical fibre tracking and virtual dissection. NeuroImage 19 (3), 545–554.

Hagmann, P., Reese, T., Tseng, W., Meuli, R., Thiran, J., Wedeen, V., 2004. Diffusion spectrum imaging tractography in complex cerebral white matter: an investigation of the centrum semiovale. Proc. Int. Soc. Magn. Reson. Med., 623 (Jul.)

Hagmann, P., Cammoun, L., Martuzzi, R., Maeder, P., Clarke, S., Thiran, J.P., Meuli, R., Hand preference and gender shape the architecture of language networks. Hum. Brain Mapp. 2006 Mar. 15, [Epub ahead of print].

Hammersley, J., Clifford, P., 1968. Markov Fields on Finite Graphs and Lattices. (unpublished manuscript).

Huang, H., Zhang, J., Jiang, H., Wakana, S., Poetscher, L., Miller, M.I., van Zijl, P.C., Hillis, A.E., Wytik, R., Mori, S., 2005. DTI tractography based parcellation of white matter: application to the mid-sagittal morphology of corpus callosum. NeuroImage 26 (1), 195–205.

Huppi, P.S., Maier, S.E., Peled, S., Zientara, G.P., Barnes, P.D., Jolesz, F.A., Volpe, J.J., 1998. Microstructural development of human newborn cerebral white matter assessed in vivo by diffusion tensor magnetic resonance imaging. Pediatr. Res. 44 (4), 584–590.

Jansons, K., Alexander, D., 2003. Persistent angular structure: new insights from diffusion magnetic resonance imaging data. Inverse Probl. 19 (5), 1031–1046.

Jansons, K., Alexander, D., 2003. Persistent angular structure: new insights from diffusion MRI data. Dummy version. Proc.-Inf. Proc. Med. Imaging 2732, 672–683.

Jonasson, L., Bresson, X., Hagmann, P., Cuisenaire, O., Meuli, R., Thiran, J.P., 2005. White matter fiber tract segmentation in DT-MRI using geometric flows. Med. Image Anal. 9 (3), 223–236.

Jonasson, L., Hagmann, P., Bresson, X., Thiran, J., Wedeen, V., 2005. Representing diffusion MRI in 5D for segmentation of white matter tracts with a level set method. In: Christensen, G.E., Sonka, M. (Eds.), LNCS. Springer-Verlag, Berlin, pp. 311–320.

Jonasson, L., Hagmann, P., Thiran, J., Wedeen, V., 2005. Fiber tracts of high angular resolution diffusion MRI are easily segmented with spectral clustering. Proc. Intl. Soc. Mag. Reson. Med. Miami Beach, p. 1310 (May).

Jones, D.K., Simmons, A., Williams, S.C., Horsfield, M.A., 1999. Non-invasive assessment of axonal fiber connectivity in the human brain via diffusion tensor MRI. Magn. Reson. Med. 42 (1), 37–41.

Kubicki, M., Park, H., Westin, C.F., Nestor, P.G., Mulkern, R.V., Maier, S.E., Niznikiewicz, M., Connor, E.E., Levitt, J.J., Frumin, M., et al., 2005. DTI and MTR abnormalities in schizophrenia: analysis of white matter integrity. NeuroImage 26 (4), 1109–1118.

Lazar, M., Alexander, A.L., 2003. An error analysis of white matter tractography methods: synthetic diffusion tensor field simulations. NeuroImage 20 (2), 1140–1153.

Lazar, M., Weinstein, D.M., Tsuruda, J.S., Hasan, K.M., Arfanakis, K., Meyerand, M.E., Badie, B., Rowley, H.A., Haughton, V., Field, A., et al., 2003. White matter tractography using diffusion tensor deflection. Hum. Brain Mapp. 18 (4), 306–321.

Lin, C.P., Wedeen, V.J., Chen, J.H., Yao, C., Tseng, W.Y., 2003. Validation of diffusion spectrum magnetic resonance imaging with manganese-enhanced rat optic tracts and ex vivo phantoms. NeuroImage 19 (3), 482–495.

Meyer, J.W., Makris, N., Bates, J.F., Caviness, V.S., Kennedy, D.N., 1999. MRI-Based topographic parcellation of human cerebral white matter. NeuroImage 9 (1), 1–17.

Mori, S., van Zijl, P.C., 2002. Fiber tracking: principles and strategies—A technical review. NMR Biomed. 15 (7–8), 468–480.

Mori, S., Crain, B.J., Chacko, V.P., van Zijl, P.C., 1999. Three-dimensional tracking of axonal projections in the brain by magnetic resonance imaging. Ann. Neurol. 45 (2), 265–269.

Pierpaoli, C., Barnett, A., Pajevic, S., Chen, R., Penix, L.R., Virta, A., Basser, P., 2001. Water diffusion changes in Wallerian degeneration and their dependence on white matter architecture. NeuroImage 13 (6 Pt. 1), 1174–1185.

Poupon, C., Mangin, J., Clark, C.A., Frouin, V., Regis, J., Le Bihan, D., Bloch, I., 2001. Towards inference of human brain connectivity from MR diffusion tensor data. Med. Image Anal. 5 (1), 1–15.

Reese, T.G., Heid, O., Weisskoff, R.M., Wedeen, V.J., 2003. Reduction of eddy-current-induced distortion in diffusion MRI using a twice-refocused spin echo. Magn. Reson. Med. 49 (1), 177–182.

Sochen, N., Kimmel, R., Malladi, R., 1998. A general framework for low level vision. IEEE Trans. Image Process. 7 (3), 310–318.

Tournier, J.D., Calamante, F., King, M.D., Gadian, D.G., Connelly, A., 2002. Limitations and requirements of diffusion tensor fiber tracking: an assessment using simulations. Magn. Reson. Med. 47 (4), 701–708.

Tournier, J.D., Calamante, F., Gadian, D.G., Connelly, A., 2004. Direct estimation of the fiber orientation density function from diffusion-weighted MRI data using spherical deconvolution. NeuroImage 23 (3), 1176–1185.

Tuch, D.S., 2004. Q-ball imaging. Magn. Reson. Med. 52 (6), 1358–1372.

Tuch, D.S., Reese, T.G., Wiegell, M.R., Makris, N., Belliveau, J.W., Wedeen, V.J., 2002. High angular resolution diffusion imaging reveals intravoxel white matter fiber heterogeneity. Magn. Reson. Med. 48 (4), 577–582.

Tuch, D.S., Reese, T.G., Wiegell, M.R., Wedeen, V.J., 2003. Diffusion MRI of complex neural architecture. Neuron 40 (5), 885–895.

Wedeen, V., 1996. Diffusion Aniostropy and White Matter Tracts. ISMRM, Boston, MA, USA (June 17–21).

Wedeen, V., Reese, T., Tuch, D., Weigel, M., Dou, J., Weiskoff, R., Chessler, D., 2000. Mapping Fiber Orientation Spectra in Cerebral White Matter with Fourier-Transform Diffusion MR. ISMRM, Denver, p. 82.

Wedeen, V.J., Hagmann, P., Tseng, W.Y., Reese, T.G., Weisskoff, R.M., 2005. Mapping complex tissue architecture with diffusion spectrum magnetic resonance imaging. Magn. Reson. Med. 54 (6), 1377–1386.

Wiegell, M.R., Larsson, H.B., Wedeen, V.J., 2000. Fiber crossing in human brain depicted with diffusion tensor MR imaging. Radiology 217 (3), 897–903.

Zhan, W., Stein, E.A., Yang, Y., 2004. Mapping the orientation of intravoxel crossing fibers based on the phase information of diffusion circular spectrum. NeuroImage 23 (4), 1358–1369.

Zhang, Y., Brady, M., Smith, S., 2001. Segmentation of brain MR images through a hidden Markov random field model and the expectation-maximization algorithm. IEEE Trans. Med. Imaging 20 (1), 45–57.

Zhukov, L., Museth, K., Breen, D., Barr, A., Whitaker, R., 2003. Level set modeling and segmentation of diffusion tensor magnetic resonance imaging brain data. J. Electron. Imaging 12 (1), 125–1133.